PUBLICATIONS OF THE ASTRONOMICAL SOCIETY OF THE PACIFIC, **121**:1180–1187, 2009 November

A Color All-Sky Panorama Image of the Milky Way

AXEL MELLINGER

Department of Physics, Central Michigan University, Mount Pleasant, MI 48859

Received 2009 August 29; accepted 2009 September 21; published 2009 October 16

ABSTRACT. This article describes the assembly of an optical (RGB) all-sky mosaic image with an image scale of $36''$pixel^{-1}, a limiting magnitude of approximately 14 mag, and an 18 bit dynamic range. Using a portable low-cost CCD camera system, 70 fields (each covering $40° \times 27°$) were imaged over a time span of 22 months from dark-sky locations in South Africa, Texas, and Michigan. The fields were photometrically calibrated against standard catalog stars. Using sky background data from the Pioneer 10 and 11 space probes, gradients resulting from artificial light pollution, airglow, and zodiacal light were eliminated, while the large-scale galactic and extragalactic background resulting from unresolved sources was preserved. The 648 megapixel image is a valuable educational tool, being able to fully utilize the resolution and dynamic range of modern full-dome planetarium projection systems.

Online material: color figures

1. INTRODUCTION

Since ancient times, astronomers have sought to draw maps of the sky, similar to their cartographer colleagues' drive to produce ever more accurate maps of the Earth. However, it was not until the invention of photography that faint, large-scale structures of nebulae and dust lanes could be faithfully reproduced. Since the late nineteenth century, several visible-light, wide-angle photographic surveys of the sky have been completed, such as E. E. Barnard's *Atlas of Selected Regions of the Milky Way* (Barnard et al. 1927); the National Geographic Society-Palomar Observatory Sky Survey of the northern sky (Minkowski & Abell 1963) and subsequently the equivalent ESO/SERC atlas of the southern sky; and more recently, the Sloan Digital Sky Survey (York et al. 2000). In addition, a Hα narrowband optical survey was compiled (Finkbeiner 2003). Very recently (after the original manuscript for the current article was submitted), the European Southern Observatory (ESO) released a Milky Way panorama image photographed by S. Brunier as part of their *Gigagalaxy Zoom* project.[1]

In 2000, the author published an all-sky color image taken on photographic 35 mm color film with a focal length of $f = 28$ mm. A total of 51 images were computer processed into a mosaic measuring 14400×7200 pixels, equivalent to an image scale of $90''$pixel^{-1} (di Cicco 1999; Kizer Whitt & Mellinger 2001). This picture is now widely used for educational purposes in planetariums, exhibitions, and textbooks; it formed the basis for a photographic star atlas (Mellinger & Hoffmann 2005), and illustrates the location of star-forming regions in the Milky Way (Mellinger 2008). With recent advances in digital projection technology, demand grew for both a higher spatial resolution and a higher dynamic range. The article describes the assembly of a 648 megapixel mosaic from more than 3000 individual CCD images.

[1] Brunier, S. 2009, ESO, http://www.gigagalaxyzoom.org.

2. DATA ACQUISITION

2.1. Hardware

2.1.1. CCD Camera

Wide-field imaging equipment based on commercial camera lenses has been successfully used in the past for, e.g., emission-line surveys (Gaustad et al. 2001) and measurements of the night-sky brightness (Shamir & Nemiroff 2005; Duriscoe et al. 2007). After exploration of several camera systems on the market, an SBIG STL-11000 CCD camera was chosen due to its

1. Moderate cost,
2. Large sensor size (36 mm $\times$ 24 mm),
3. Antiblooming gate (eliminating the need for software deblooming), and
4. Compact construction (low back focus, allowing the use of 35 mm camera lenses).

The camera uses a Kodak KAI-11002 chip, a $4008\ (H) \times 2672\ (V)$ progressive scan interline CCD image sensor with an antiblooming gate (Eastman Kodak Company 2006). It uses microlenses to enhance its quantum efficiency by directing light to the active pixel areas. Drawbacks of this design include nonlinearity and angular quantum-efficiency variations, and are addressed in §§ 3.1 and 3.2.

2.1.2. Lens

The camera was fitted with a Minolta MD $1.4/50$ mm lens originally used on a 35 mm format film-based single-lens reflex camera. To improve the image quality, the lens was stopped down to f/4 for all exposures.

2.1.3. Filters

As the principal purpose of the panorama image is to create a visual representation of colors in the sky, an RGB filter set (Astronomik Type 2c) was used instead of the Johnson $UBVR$ filters common in photometry. The transmission curves are shown in Figure 1.

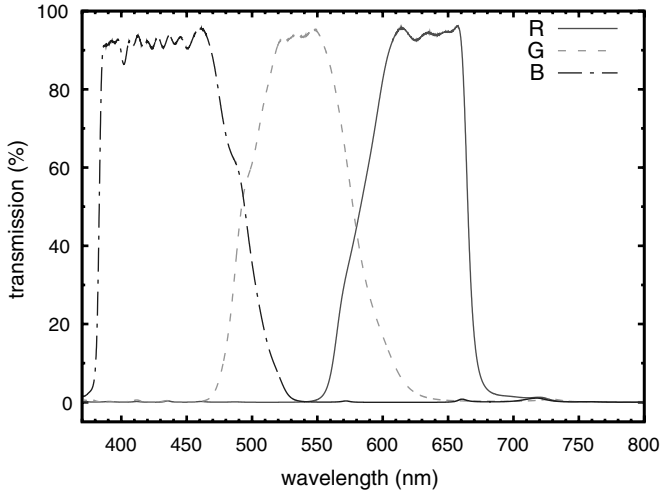

FIG. 1.—Transmission curves of the Astronomik RGB filters.

2.2. Field Selection

The KAI-11002 chip has an active area of 36×24 mm^2, resulting in a field of view of approximately $40° \times 27°$ at a focal length of $f = 50$ mm. Due to the location of the mounting thread on the camera, a "portrait" orientation of the camera was chosen, with the long side of the chip being parallel to circles of constant right ascension. To ensure a seamless mosaic, adjacent fields had to overlap each other by at least 15% of the respective offset in right ascension or declination. With these constraints, a coverage pattern (Fig. 2) was developed by way of trial and error. The pattern consists of five rings of frames centered at declinations of $+62°$, $+32°$, $0°$, $-32°$, and $-62°$, in addition to two fields centered at the celestial poles ($\pm 90°$). The number of fields and offsets in right ascension are listed in Table 1.

2.3. Exposure Times

In order to increase the dynamic range beyond the 16 bits of the camera's analog-to-digital converter (of which approximately 12 bits provide data above the noise level), three different exposure times (240 s, 15 s, and 0.5 s) were used. Five frames were taken for each exposure time and filter setting.

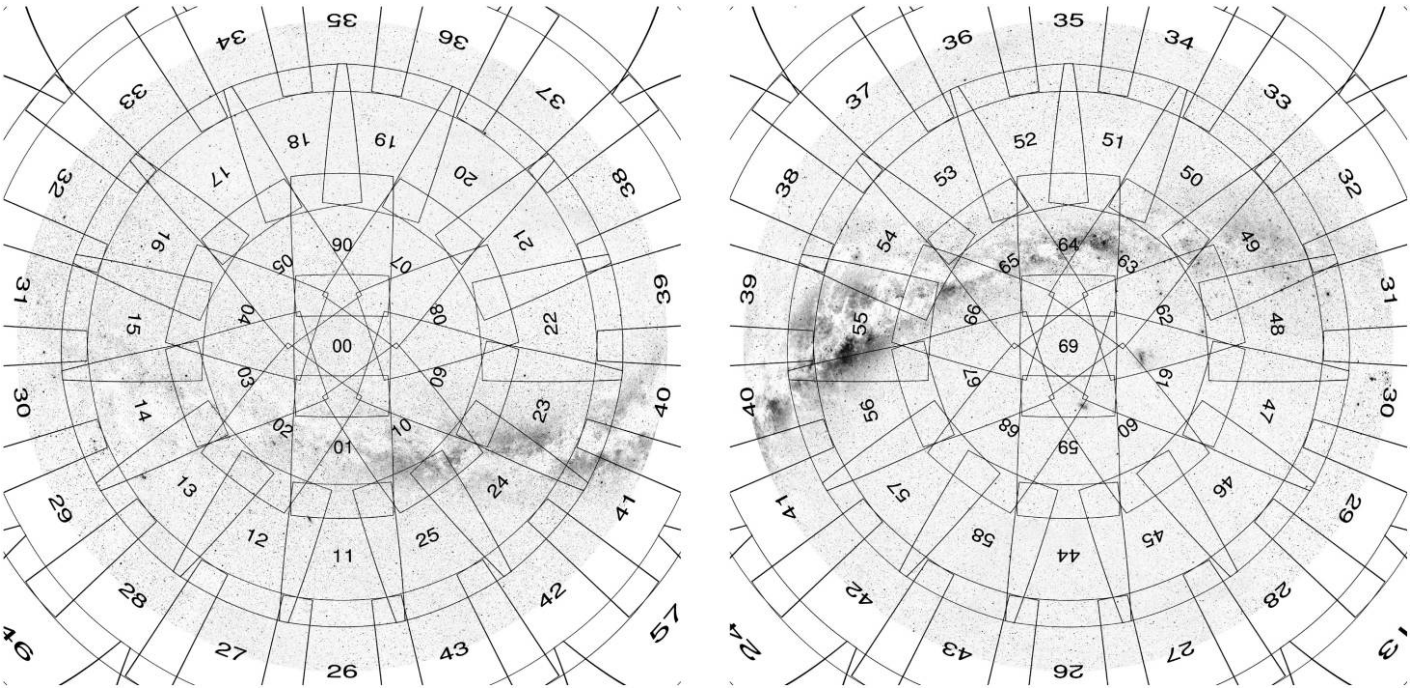

FIG. 2.—Northern (*left*) and southern (*right*) hemisphere coverage maps of the 70 fields. See the electronic edition of the *PASP* for a color version of this figure.

TABLE 1
DECLINATION OF FIELD CENTERS AND R.A. OFFSETS

Field Number(s)	Decl. (δ_c)	R.A. Offset
0	+90°	
1–10	+62°	02 24
11–25	+32°	01 36
26–43	0°	01 20
44–58	−32°	01 36
59–68	−62°	02 24
69	−90°	

2.4. Sites

The fields centered at declinations −90°, −62°, −32°, and 0° were taken in 2007 October and 2008 March/April from dark-sky locations in South Africa (Tables 2 and 3), while the northern hemisphere images (declinations +32°, +62°, and +90°) were taken between 2008 December and 2009 August from dark-sky locations in Texas and Michigan in the US.

3. DATA PROCESSING

3.1. Nonlinearity Correction

The use of a CCD sensor with an antiblooming gate often comes at the expense of linearity (Duriscoe et al. 2007). To test the sensor linearity, a uniform white target illuminated by a light-emitting diode (LED) operated in constant-current mode was photographed with a series of exposure times ranging from 0.02 to 30 s. To check for variations in the LED intensity, two series of exposures (one from short to long exposure times, the other from long to short) was taken. After dark-frame subtraction, the flux in a field measuring 200 × 200 pixels at the image center was measured using the IRAF `imstat` task. The test revealed a significant deviation from a linear response for a signal as low as 15000 ADU s pixel^{-1}, well below the full-well depth of approximately 60000 ADU s pixel^{-1} (Fig. 3). However, the observed signal as a function of illumination could be well represented by the quadratic equation

$$S(E) = a_1 E + a_2 E^2, \tag{1}$$

where E is the exposure (product of light intensity and exposure time) and S is the measured signal. Based on these data, a nonlinearity correction was developed as follows: Solving equation (1) for E yields

$$E = \frac{-a_1 + \sqrt{a_1^2 + 4a_2 S}}{2a_2}.$$

The corrected (linearized) signal is then

$$S' = a_1 E = \frac{1}{2\alpha}(\sqrt{1 + 4\alpha S} - 1), \tag{2}$$

where

$$\alpha := \frac{a_2}{a_1^2}. \tag{3}$$

From a least-squares fit, α was determined as -7.5334×10^{-7} ADU^{-1}. This function was applied to all raw images, including the flat frames (but not the dark frames, due to their low ADU values).

3.2. Preprocessing

The standard preprocessing steps (dark-frame subtraction, masking of bad pixels, division by flat frame) were applied to all images. Due to its microlenses, the angular quantum efficiency of the CCD chip depends upon the angle of incidence. This angular profile in turn is a function of the wavelength (Eastman Kodak Company 2006). Hence, flat frames taken through the R, G, and B filters differ significantly (Fig. 4).

Depending on the spectral distribution of the sky background, this wavelength-dependent sensitivity of the camera system may lead to residual gradients, even with proper flat-frame calibration. However, these gradients were later eliminated by the background-subtraction procedure detailed in § 3.4.3.

TABLE 2
OBSERVATION SITES

Site Abbreviation	Site	Latitude	Longitude	Elevation (m)
CEDB	Cederberg Observatory, Western Cape, South Africa	32°29′58″ S	19°15′10″ E	865
KOOR	Koornlandskloof Guest Farm, Northern Cape, South Africa	32°13′34″ S	20°20′48″ E	1273
BBE1	Big Bend National Park, Texas (Rio Grande Village)	29°10′45″ N	102°57′20″ W	556
BBE2	Big Bend National Park, Texas (Grapevine Hills)	29°22′40″ N	103°13′16″ W	1029
BBE3	Big Bend National Park, Texas (Terlingua Abajo)	29°11′57″ N	103°36′14″ W	677
FTDV	Near Fort Davis, Texas	30°36′54″ N	103°58′38″ W	1580
FRMI	Filion Rd. near Bay Port, MI	43°53′12″ N	83°19′53″ W	177
MCLL	McCollum Lake, MI	44°46′13″ N	83°54′05″ W	285
HNFO	Huron National Forest, MI	44°39′09″ N	83°51′47″ W	290

TABLE 3
FIELD LIST

Field	Site	Image Center R.A.	Image Center Decl.	Start of First Exposure (UTC) Date	Start of First Exposure (UTC) Time
00	BBE2	00 00	+90°	2008 Dec 27	05:47:01
01	BBE1	00 00	+62°	2008 Dec 26	03:38:41
02	BBE1	02 24	+62°	2008 Dec 26	05:15:59
03	BBE2	04 48	+62°	2008 Dec 26	03:56:00
04	FTDV	07 12	+62°	2008 Dec 30	05:54:20
05	BBE1	09 36	+62°	2008 Dec 25	11:03:10
06	BBE2	12 00	+62°	2008 Dec 27	10:58:39
07	BBE3	14 24	+62°	2008 Dec 28	09:28:14
08	MCLL	16 48	+62°	2009 May 25	03:05:09
09	HNFO	19 12	+62°	2009 Jul 21	03:02:54
10	BBE2	21 36	+62°	2008 Dec 27	02:14:30
11	BBE1	00 00	+32°	2008 Dec 23	01:56:22
12	BBE1	01 36	+32°	2008 Dec 23	03:42:07
13	BBE1	03 12	+32°	2008 Dec 23	05:28:04
14	BBE1	04 48	+32°	2008 Dec 24	03:56:22
15	BBE1	06 24	+32°	2008 Dec 23	07:11:20
16	BBE1	08 00	+32°	2008 Dec 23	08:53:32
17	BBE1	09 36	+32°	2008 Dec 24	07:24:30
18	BBE1	11 12	+32°	2008 Dec 24	09:04:45
19	BBE1	12 48	+32°	2008 Dec 24	10:36:04
20	BBE3	14 24	+32°	2008 Dec 28	11:04:58
21	MCLL	16 00	+32°	2009 May 25	04:48:28
22	MCLL	17 36	+32°	2009 May 25	06:14:52
23	HNFO	19 12	+32°	2009 Jul 21	04:45:24
24	HNFO	20 48	+32°	2009 Aug 16	03:03:46
25	BBE3	22 24	+32°	2008 Dec 28	01:36:06
26	KOOR	00 00	00°	2007 Oct 10	20:12:49
27	KOOR	01 20	00°	2007 Oct 12	20:21:02
28	KOOR	02 40	00°	2007 Oct 09	23:55:27
29	KOOR	04 00	00°	2007 Oct 10	01:56:45
30	KOOR	05 20	00°	2007 Oct 13	01:40:04
31	KOOR	06 40	00°	2008 Apr 07	17:48:53
32	KOOR	08 00	00°	2008 Apr 08	17:50:36
33	KOOR	09 20	00°	2008 Apr 07	19:17:06
34	KOOR	10 40	00°	2008 Apr 05	19:43:51
34b	FRMI	10 40	00°	2009 Apr 25	02:47:36
35	KOOR	12 00	00°	2008 Apr 05	20:46:28
36	KOOR	13 20	00°	2008 Apr 05	22:10:40
36b	FTDV	13 20	00°	2008 Dec 30	11:18:56
37	KOOR	14 60	00°	2008 Apr 07	21:13:17
38	KOOR	16 00	00°	2008 Apr 07	22:56:53
39	KOOR	17 20	00°	2008 Apr 08	00:34:04
40	KOOR	18 40	00°	2007 Oct 12	18:19:46
41	KOOR	20 00	00°	2007 Oct 09	18:20:18
42	KOOR	21 20	00°	2007 Oct 09	20:02:07
43	KOOR	22 40	00°	2007 Oct 09	21:40:59
44	KROM	00 00	−32°	2007 Oct 04	20:27:47
45	KROM	01 36	−32°	2007 Oct 04	22:22:48
46	KROM	03 12	−32°	2007 Oct 05	00:05:33
47	KOOR	04 48	−32°	2007 Oct 12	22:21:22
48	KOOR	06 24	−32°	2007 Oct 12	23:59:58
49	CEDB	08 00	−32°	2008 Mar 29	19:14:05
49	KOOR	08 00	−32°	2008 Apr 08	19:37:29
50	CEDB	09 36	−32°	2008 Mar 29	21:23:53
51	CEDB	11 24	−32°	2008 Mar 30	19:56:46
51	KOOR	11 24	−32°	2008 Apr 03	20:18:02
52	KOOR	12 48	−32°	2008 Apr 08	22:58:17
53	KOOR	14 24	−32°	2008 Apr 09	00:46:19
54	KOOR	16 00	−32°	2008 Apr 05	23:45:24
55	KOOR	17 36	−32°	2008 Apr 06	01:34:05
55b	KOOR	17 36	−32°	2008 Apr 08	02:38:10
56	CEDB	19 12	−32°	2007 Oct 05	18:06:31
57	CEDB	20 48	−32°	2007 Oct 05	20:02:16
58	KROM	22 24	−32°	2007 Oct 04	18:39:01
59	CEDB	00 00	−62°	2007 Oct 05	22:01:34
60	CEDB	02 24	−62°	2007 Oct 05	23:45:45
61	KOOR	04 48	−62°	2008 Apr 05	17:58:42
62	KOOR	07 12	−62°	2008 Apr 03	18:01:53
63	KOOR	09 36	−62°	2008 Apr 08	20:55:47
64	KOOR	12 00	−62°	2008 Apr 01	23:47:05
65	KOOR	14 24	−62°	2008 Apr 03	23:26:34
66	KOOR	16 48	−62°	2008 Apr 04	01:03:40
67	KOOR	19 12	−62°	2007 Oct 08	18:13:48
68	KOOR	21 36	−62°	2007 Oct 08	19:52:48
69	KOOR	00 00	−90°	2007 Oct 08	21:41:51

NOTE.—A few images were affected by the presence of bright planets or satellite trails and were retaken. In these cases, data from both sets of data was used for correcting the defects.

Next, the images were upsampled by a factor of 3. Although it increases the file size by 9×, this step was found to be necessary in order to minimize the loss of resolution in subsequent resampling with bilinear interpolation. Higher-order interpolation methods, such as bicubic or Lanczos resampling, could not be used as they introduce ringing artifacts in undersampled images.

3.3. Astrometric Calibration

Wide-angle imaging requires careful astrometric calibration, taking into account distortions of the camera lens beyond a simple gnomonic projection. In each raw image, up to 1500 reference stars were automatically selected using the Source Extractor software (Bertin & Arnouts 1996) and pattern matched against sources in the Hubble Guide Star Catalog 1.2 (Morrison et al. 2001). The pattern-matching algorithm was invented by Valdes et al. (1995) and implemented in C by Richmond (2008). With these reference stars, an astrometric solution was calculated using custom software, and a world coordinate system (WCS) header was added to the FITS file. For each field, all images with a common exposure time and filter setting were then resampled and co-added with the SWarp software (Bertin et al. 2002). Finally, all pixels in the 240 s frames that were masked as saturated (cf. § 3.2) were replaced by scaled pixel values from the 15 s or 0.5 s frames using the IRAF `imexpr` task.

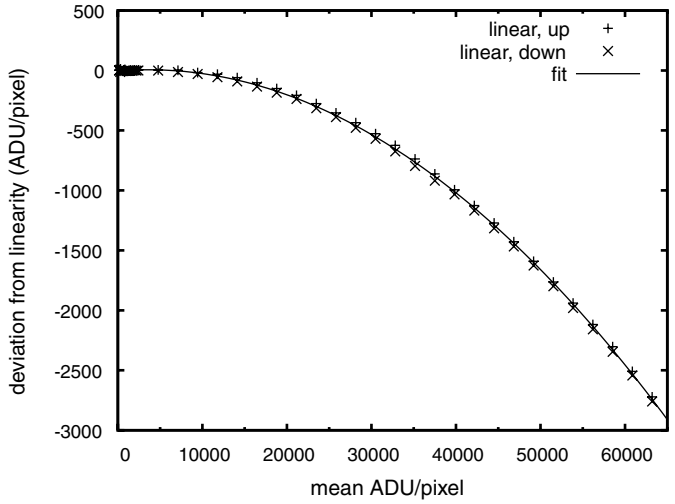

FIG. 3.—Nonlinearity of the STL-11000 camera obtained in laboratory tests with a constant-current LED light source. The *solid line* shows the least-squares fit according to eq. (1).

3.4. Photometric Calibration

A major problem was the photometric calibration of the individual fields. A straight combination without photometric corrections yields a patchy-looking mosaic, as shown in Figure 5. Clearly, the sky background level varies significantly between fields, and some fields exhibit strong intrafield background gradients. Moreover, differences in atmospheric transparency may cause the recorded flux I of a star to vary between two frames.

3.4.1. Contributions to the Sky Background

The diffuse night-sky background has a variety of sources (see Leinert et al. 1998 for an in-depth discussion):

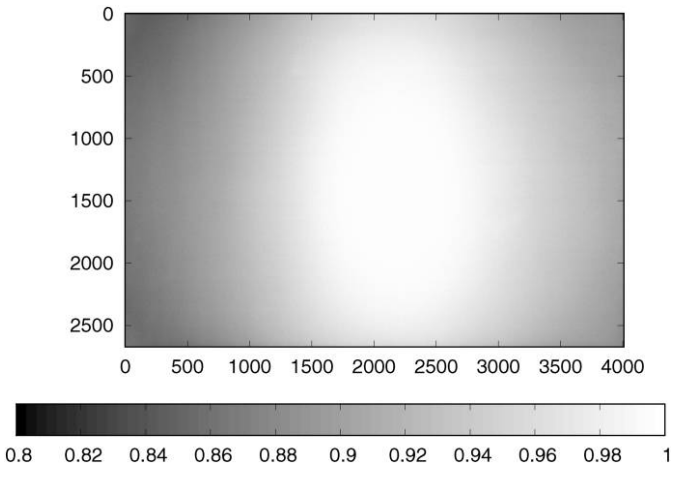

FIG. 4.—Ratio of R and G flat fields.

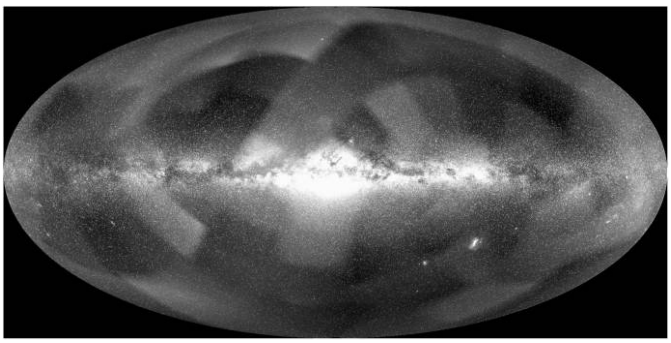

FIG. 5.—R channel mosaic, combined without photometric calibration and background subtraction. There are strong variations in the background level, as well as intrafield gradients.

1. *Light pollution* ($I_{\rm LP}$). Although most images were taken from dark-sky sites (class 1 on Bortle's scale (Bortle 2001)), time constraints dictated that some fields were taken from sites with slight artificial light pollution (the Michigan sites have Bortle class 2 or 3). In addition, again due to time constraints, some images were taken in the evening sky before the end of astronomical twilight, or in the morning sky past the beginning of astronomical twilight.

2. *Airglow* ($I_{\rm A}$). In the absence of light pollution, airglow is the largest contributor to the night sky brightness (Leinert et al. 1998). In the visible spectrum, the main sources are atmospheric O_2 (for wavelengths $\lambda < 430$ nm) and OH (for $\lambda > 520$ nm). Air glow is highly variable both in spatial distribution and in time.

3. *Zodiacal light* ($I_{\rm ZL}$). Zodiacal light is sunlight scattered by interplanetary dust particles. Near the ecliptic poles, its intensity in the visible spectrum is typically 2–4 times weaker than airglow, but it gains significantly as the field of view gets closer to the sun. Due to its spatial confinement to the ecliptic region, it can cause strong background gradients in wide-field images.

4. *Tropospheric scattering* ($I_{\rm sca}$). Starlight as well as airglow and zodiacal light are scattered in the troposphere. High clouds as well as high humidity at ground level can enhance scattering and lead to halos around bright stars.

5. *Integrated starlight* ($I_{\rm ISL}$). Another contribution to the sky brightness is the light from unresolved stars. At visible wavelengths, it is dominated by main-sequence stars (Leinert et al. 1998).

6. *Diffuse galactic light* ($I_{\rm DGL}$). Diffuse galactic light (DGL) is produced when starlight is scattered by dust grains in interstellar space.

7. *Extragalactic background light* ($I_{\rm EBL}$). Light from galaxies that are not individually detected.

Many of these contributions to the night-sky brightness are undesirable in an all-sky mosaic image. Light pollution, airglow, zodiacal light, and tropospheric scattering vary between individual fields, as well as within a field, and thus should be removed

in the calibration process. However, the contribution from unresolved stars and the diffuse galactic light are features of the Milky Way and should be preserved, together with any extragalactic background. This creates a major calibration problem, as we need to decide on how much of the local background is caused by unwanted sources (1–4 in list) or galactic and extragalactic contributions to be retained (5–7 in list). This problem has plagued a number of ground-based studies of the galactic background (Leinert et al. 1998). However, these effects can be separated using space-borne visual photometry data from the Imaging Photopolarimeters (IPPs) onboard the Pioneer 10 and 11 space probes. Their data were obviously not contaminated by terrestrial sources, and the zodiacal light contribution became negligible for distances above 3.3 AU (Gordon 1997; Gordon et al. 1998).

The photometric calibration of the all-sky image was performed in two steps:

3.4.2. Standard Star Processing

For each field and color channel, a list of several hundred reference stars (that included their equatorial coordinates, fluxes S (in ADU), and local backgrounds β) was generated using Source Extractor and matched against the Yale Bright Star (YBS) Catalog.[2] Typically, 100…120 matches were found. The reference star magnitude V and the measured flux are related via

$$V = Q - 2.5 \lg S + \epsilon(B - V), \tag{4}$$

where Q is the instrumental zero point (including effects of atmospheric extinction) and $(B - V)$ is the color index from the YBS Catalog. Q and ϵ were then determined via a least-squares fit. A typical plot of calibrated V magnitudes (calculated according to eq. [5]) versus YBS catalog magnitudes is shown in Figure 6. As expected, the spectral correction parameter ϵ was close to -1 for the B channel frames and close to 0 for the G channel, while values of approximately $+0.3$ were typical for the R channel. The ADU units were then converted to $S_{10}(V)$ units commonly used for measuring surface brightness (Sparrow & Weinberg 1976). One $S_{10}(V)$ unit represents the sky brightness resulting from one tenth-magnitude star per square degree. Thus,

$$1\ S_{10}(V) = \kappa^2 10^{0.4(Q-10)}\ \text{ADU}, \tag{5}$$

where κ is the image scale in degrees per pixel.

3.4.3. Background Subtraction

According to the discussion at the start of § 3.4, the total light intensity seen by a CCD pixel is

[2] VizieR Online Data Catalog, 5050 (Hoffleit, D., & Warren, Jr., W. H., 1995).

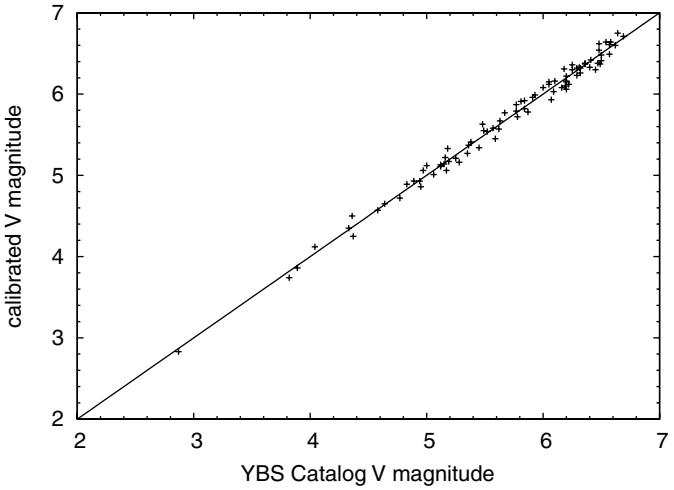

FIG. 6.—Calibrated V magnitudes (calculated the measured flux via to eq. (5)) vs. YBS catalog magnitudes.

$$I = S + I_{\text{bad}} + I_{\text{good}}, \tag{6}$$

where S is the flux due to point sources or resolved diffuse objects, $I_{\text{bad}} = I_{\text{LP}} + I_{\text{A}} + I_{\text{ZL}} + I_{\text{sca}}$ is the unwanted background contribution from terrestrial and solar system sources, and $I_{\text{good}} = I_{\text{ISL}} + I_{\text{DGL}} + I_{\text{EBL}}$ is the galactic and extragalactic background to be retained in the image. Since I_{good} is known from the Pioneer 10/11 data (Gordon et al. 1998), the spatial distribution of I_{bad} can be modeled by fitting a surface to $(I - I_{\text{good}})$.

Unfortunately, the high-resolution background data by Gordon et al. (1998) do not cover the entire sky; they excluded the data contaminated with scattered sunlight, taken within 70° of the Sun for Pioneer 10 and within 45° for Pioneer 11, respectively. Leinert et al. (1998) provide some additional data points on a $10° \times 10°$ grid; the other missing data were interpolated using a bicubic spline function. Some local median filtering was applied in order to remove small-scale artifacts in the data.

With the Pioneer data providing I_{good}, the "bad" background was estimated by applying a strong median filter to $(I - I_{\text{good}}) = (S + I_{\text{bad}})$. Subtracting I_{bad} from I then yields the desired sum of $S + I_{\text{good}}$. This approach also eliminates any residual gradient from the wavelength-dependent angular response of the camera system (cf. § 3.2).

3.5. Final Assembly and Color Processing

The scaled and background-corrected images were resampled and co-added using SWarp. This software can be configured to generate a range of projections defined in the FITS/WCS standard (Calabretta & Greisen 2002), including Hammer-Aitoff, equidistant cylindrical (plate carrée), and equidistant azimuthal. In addition, a number of target coordinate systems (equatorial, galactic, etc.) are available.

The resulting R, G, and B fits images were converted to a single RGB TIFF file using the STIFF software.[3] This program converts the 32 bit floating-point brightness values to 8 bit numbers by applying a nonlinear transfer function to the luminance channel only. This way, bright objects do not appear "burnt out" as is often seen in images where the transfer function is applied directly to the R, G, and B channels (Lupton et al. 2004).

4. RESULTS

The above procedure created a $360° \times 180°$ panorama image of the entire sky at a scale of $36''\text{pixel}^{-1}$, equivalent to a size of 36000×18000 pixels. With each pixel represented by a 32 bit (single precision) floating-point number, each color channel is approximately 2.5 gigabytes in size. The faintest visible stars are approximately 14 mag, while only stars brighter than $+0.7$ mag are saturated. (This saturation could have been avoided by reducing the shortest exposure time below 0.5 s, but this would have reduced the number of reference stars suitable for astrometric calibration.) Hence, the dynamic range is approximately 18 bits.

A low-resolution color image of the panorama is shown in Figure 7. A zoomable Mercator projection can be seen on the author's web site.[4] The image provides a detailed view of large-scale galactic structures, such as a halo of unresolved stars extending to $b \leq \pm 25°$, and numerous dark clouds. Note the strong reddening of starlight in the Ophiuchus/Scorpius region of the Milky Way. In the earlier panorama (Mellinger & Hoffmann 2005), many of these details are missing due to the rather aggressive flat-fielding employed at the time. In a historical contect, the panorama image may be compared to the hand-drawn maps of Gaposchkin (1957) and the first all-sky image in Aitoff projection by Lundmark,[5] as well as early photometric studies of the Milky Way (Pannekoek et al. 1949).

Besides galactic stars and nebulae, and some brighter extragalactic objects (most notably, the Magellanic Clouds and the Andromeda galaxy), the panorama image also shows a number of solar system objects. In most cases, the bright planets could be avoided by scheduling the exposures for times when no planet was near the field of view. No attempt was made to remove or avoid solar system objects invisible to the naked eye.

Several of the raw images taken from South Africa in 2008 April exhibit trails of geosynchronous satellites. At that time (2–3 weeks after the southern hemisphere fall equinox), sunlight glinting off reflective surfaces is directed toward the southern hemisphere, causing the satellite to brighten by several magnitudes. As the camera was tracking the stars, each satellite left a 1° trail on the 240 s exposures. Median combining the raw frames eliminated most of the satellite trails; however, fields #34 and 36 had to be retaken as the blending of multiple trails caused them to be quite apparent even in the combined images.

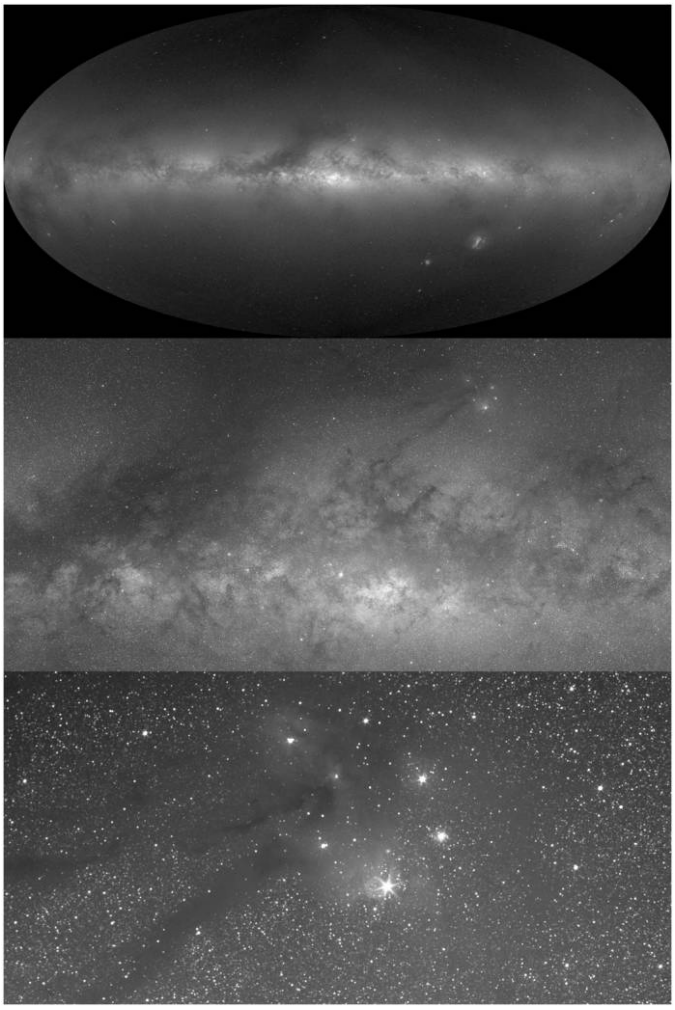

FIG. 7.—RGB mosaic, combined with photometric calibration and background subtraction. *Top:* entire sky in Hammer-Aitoff projection. *Middle:* enlarged view of the central Milky Way. *Bottom:* full-scale view of the Antares/ρ Oph region. See the electronic edition of the *PASP* for a color version of this figure.

A comparison with the very recently released ESO *Gigagalaxy Zoom* Milky Way panorama[6] shows that both images were photographed at the same focal length of $f = 50$ mm. Brunier made his panorama with a Nikon D3 camera which has a non-cooled 36×23.9 mm^2 sensor with 4256×2832 pixels and a color filter array (CFA). Its pixels are about 6% smaller than those of the STL-11000; however, the demosaicing process required for CFA sensors (Gunturk et al. 2005) would lead to

[3] Bertin, E. 2008, STIFF v. 1.12 User's Guide, http://astromatic.iap.fr/software/stiff/.

[4] Milky Way Panorama 2.0, 2009, http://home.arcor.de/axel.mellinger/.

[5] Lundmark, K. 1955, The Lund Panorama of the Milky Way, http://www.astro.lu.se/Resources/Vintergatan/.

[6] Brunier, S. 2009, ESO, http://www.gigagalaxyzoom.org.

some loss of spatial resolution. No information on the dynamic range and photometric calibration of the ESO image is currently available, although the use of a single exposure time (6 minutes) suggests a dynamic range significantly lower than the 18 bit range of the image described in this article.

5. APPLICATIONS

First and foremost, the all-sky mosaic image is expected to be a valuable educational tool. Modern digital full-dome planetarium projection systems offer 12 bits of resolution per color channel, with 16 bits not too far down the road. With an 18 bit dynamic range, it will be possible to blend over from a view showing only the brightest stars (simulating the view in a light-polluted environment) to a full display of the faint star clouds and nebulae in our Milky Way. The resolution of $36''\text{pixel}^{-1}$ ensures crisp star images that will be limited by the resolution of the projection equipment and the observer's eye, rather than the image data. As the size of the image (7.5 gigabytes for a 32 bit floating-point representation) may exceed the capabilities of some personal computers, an OpenEXR version is in preparation. This file format uses 16 bit (half-precision) floating-point numbers for storing the image data,[7] thus reducing the file size by a factor of 2.

In addition to its use in education, the image is also of scientific value, as it supplements earlier work on the surface photometry of the Milky Way, such as Hoffmann et al. (1998). As an example, studies of the night sky background (see, e.g., Duriscoe et al. 2007) need to discern between man-made light pollution and natural contributions to the sky brightness (a problem very similar to the one encountered in the present work), and would thus benefit from photometric data on the Milky Way brightness.

[7] Kainz, F. 2009, Technical Introduction to OpenEXR, Industrial Light & Magic, http://www.openexr.com.

REFERENCES

Barnard, E. E., Frost, E. B., & Calvert, M. R. 1927, ed., A Photographic Atlas of Selected Regions of the Milky Way (Washington, DC: Carnegie Institution)

Bertin, E., & Arnouts, S. 1996, A&AS, 117, 393

Bertin, E., Mellier, Y., Radovich, M., Missonnier, G., Didelon, P., & Morin, B. 2002, in ASP Conf. Ser. 281, Astronomical Data Analysis Software and Systems XI, ed. Bohlender, D. A., Durand, D., & Handley, T. H., 228

Bortle, J. E. 2001, S&T, 101, 126

Calabretta, M. R., & Greisen, E. W. 2002, A&A, 395, 1077

di Cicco, D. 1999, S&T, 98, 137

Duriscoe, D. M., Luginbuhl, C. B., & Moore, C. A. 2007, PASP, 119, 192

Eastman Kodak Company, 2006, Application note: KODAK KAI-11002 Image Sensor, Revision 1.0 MTD/PS-0938

Finkbeiner, D. P. 2003, ApJS, 146, 407

Gaposchkin, S. 1957, in Vistas in Astronomy, vol. III, 289–295

Gaustad, J. E., McCullough, P. R., Rosing, W., & Van Buren, D. 2001, PASP, 113, 1326

Gordon, K. D. 1997, Ph.D. thesis, Univ. of Toledo

Gordon, K. D., Witt, A. N., & Friedmann, B. C. 1998, ApJ, 498, 522

Gunturk, B. K., Glotzbach, J., Altunbasak, Y., Schafer, R. W., & Mersereau, R. M. 2005, IEEE Signal Proc. Mag., 22, 44

Hoffmann, B., Tappert, C., Schlosser, W., Schmidt-Kaler, T., Kimeswenger, S., Seidensticker, K., Schmidtobreick, L., & Hovest, W. 1998, A&AS, 128, 417

Kizer Whitt, K., & Mellinger, A. 2001, Astronomy, 29, 58

Leinert, C., et al. 1998, A&AS, 127, 1

Lupton, R., Blanton, M. R., Fekete, G., Hogg, D. W., O'Mullane, W., Szalay, A., & Wherry, N. 2004, PASP, 116, 133

Mellinger, A. 2008, in Handbook of Star Forming Regions: The Northern Sky, ed. Reipurth, B. (vol. I, San Francisco: ASP)

Mellinger, A., & Hoffmann, S. M. 2005, The New Atlas of the Stars (Richmond Hill, Ontario: Firefly Books)

Minkowski, R. L., & Abell, G. O. 1963, The National Geographic Society-Palomar Observatory Sky Survey, ed. Strand, K. A. (Chicago: Univ. Chicago Press), 481

Morrison, J. E., Röser, S., McLean, B., Bucciarelli, B., & Lasker, B. 2001, AJ, 121, 1752

Pannekoek, A., Koelbloed, D., & Voute, J. G. E. G. 1949 (vol. 9; Amsterdam: Publications of the Astronomical Institute of the University of Amsterdam) 1

Richmond, M. 2008, Match–A Program for Matching Star Lists, http://spiff.rit.edu/match/

Shamir, L., & Nemiroff, R. J. 2005, PASP, 117, 972

Sparrow, J. G., & Weinberg, J. L. 1976, in Lecture Notes in Physics 48, Interplanetary Dust and Zodiacal Light, ed. Elsaesser, H., & Fechtig, H. (Berlin: Springer), 41

Valdes, F. G., Campusano, L. E., Velasquez, J. D., & Stetson, P. B. 1995, PASP, 107, 1119

York, D. G., et al. 2000, AJ, 120, 1579